Enhancing PET/CT Assessment with Porous 3D-Printed Grids – A Pilot Study

Sai Kiran Kumar Nalla[1], Quentin Maronnier[3], John A. Kennedy[4,5], Tala Palchan-Hazan[4], Olivier Caselles[2,3] *

1. Institut universitaire du cancer de Toulouse - IUTC, Université de Toulouse, 31400 Toulouse, France
2. Tachyons SAS, Toulouse, France
3. Department of Medical Physics, Institut Claudius Regaud, Toulouse, France
4. Department of Nuclear Medicine, Rambam Health Care Campus, P.O.B. 9602, 3109601 Haifa, Israel
5. Ruth and Bruce Rappaport Faculty of Medicine, Technion Israel Institute of Technology, Haifa, Israel

***Correspondance :** Olivier Caselles (**caselles.olivier@iuct-oncopole.fr**)

ORCID IDS :

Sai Kiran Kumar Nalla : 0000-0002-8044-6330

Quentin Marronnier : 0000-0002-2266-9122

John A Kenedy**:** 0000-0002-2043-4397

Tala Palchan-Hazan: 0009-0004-2632-1168

Olivier Caselles: 0000-0002-5404-5066

NOTE: This preprint reports new research that is not certified by peer review and should not be used to guide clinical practice.

Abstract:

Phantom Experiments are widely used for standardisation, but currently used practices to do not resonate with clinical reality and follow a complicated phantom preparation protocol. 3D printing can help overcome some of these limitations by optimizing preparatory methods and improving phantom features. This work proposes employing 3D-printed porous grids as an alternative to fillable spheres. The qualitative and quantitative characterisation of these grids is presented. 4 cm Acrylonitrile Butadiene Styrene (ABS) cubic grids with varying pore distance (5 mm, 7 mm, 10 mm) and Solidity (50%, 60%, 70%) were printed. Spherical targets of 10, 15 and 20 mm were also incorporated for quantitation and detectability. Grids were immersed in a NEMA Flangeless Jaszczak Phantom, later filled with distilled water, soap and [^{18}F] fluorodeoxyglucose (FDG). Five consecutive acquisitions were repeated on five different days (Day 0,1,4-6) using Discovery MI PET/CT. Hounsfeild Units (HU), Recovery Coefficient (RC) and Dilution Coefficient (DC) were the metrics used for analysis. Friedman test was utilized to study global statistical significance across days. Additionally, Wilcoxon with Bonferroni correction provided insights into pairwise differences between days. HU enhancement was observed in the CT over the days with values reaching closer to water (0). 5mm pore distance grid produced the best resolution. PET quantification showed consistent results across trials, confirming robustness. Achieved contrasts were 1.93 ± 0.14, 2.44 ± 0.2 & 3.01 ± 0.08 against 2, 2.5 and 3.33 (Theoretical). Observed RC were in range of 0.4 – 1.2. Friedman *p*-values (0.98 & 0.93) suggested strong correlations across the days. Wilcoxon revealed that Day 1 vs Day 5 had best comparable results. 3D-printed grids offer a reliable, reproducible alternative for PET/CT assessment. Six times higher number of targets were produced in one phantom with single tracer administration. CT attenuation improved significantly while maintaining PET performance.

Keywords: Additive Manufacturing, Fused Deposition Modeling, Quantitative PET CT, Nuclear Medicine, Rapid Prototyping, Radionuclide Imaging

NOTE: This preprint reports new research that is not certified by peer review and should not be used to guide clinical practice.

1. Introduction:

Quality control (QC) in Nuclear Medicine (NM) is an important field focusing on accuracy, reliability, and safety of both diagnostic and therapeutic procedures, particularly in fused modalities like Positron Emission Tomography / Computed Tomography (PET/CT) and Single Photon Emission Computed Tomography / Computed Tomography (SPECT/CT) (1–3). A large variety of phantoms prescribed by the *National Electrical Manufacturers Association (NEMA) or International Electrotechnical Commission (IEC)* are available, among others: Jaszczak, NEMA, Hoffman brain, and IEC body phantoms. These phantoms usually contain multiple compartments and inserts like acrylic spheres to simulate lesions. By carefully filling these compartments and inserts with radiotracer activity concentration, these phantoms support the assessment of detection and quantitation (4–6). One of the notable limitations in the conventional protocols using acrylic spheres in QC is that minor variations in activity concentrations on the PET images accompanied by the "wall effect": (added contrast coming from the solid walls of the sphere are associated with edge artefacts) reduce the clinical relevance of such inserts (7–10). Moreover, the number of features and their positions are fixed (11–13); therefore, assessment is constrained to specific predetermined locations with limited customizability in the imaging field of view (FOV). The time taken for phantom preparation is also long due to multi compartment filling which opens potential for preparation errors (6,14). Often this is frequently translated into higher radiation exposure for technicians and physicists performing such tests and further limits the practicality of frequent experiments (15).

While useful for standardization, phantom experiments fail to replicate complex anatomical variability seen in clinical reality (2). This limitation becomes increasingly challenging as PET/CT scanners resolution improve significantly with each generation. Necessity for protocols to be able to test smaller lesions (<1cm) or heterogeneity is increasing (6). Also, the lack of patient-dependent variability and realistic material properties within standard phantoms limits their usage (16,17) to assess AI based algorithms. 3D Printing with its versatile potential has been reported previously to address the

NOTE: This preprint reports new research that is not certified by peer review and should not be used to guide clinical practice.

shortcomings and bridge the gaps between physics and physicians (18–32). In the context of PET/ CT applications, 3D printing has been used to create complex anatomical phantoms closer to clinics with customizable lesions, thus complementing the features of modern scanning technology (24,33,34) . The two major cost-effective methods of 3D printing namely Fused Deposition Modelling (FDM) and Stereolithography (SLA), were widely utilized in research for the fabrication of phantoms. Studies using Polyjet printing have also been reported for (24,26,32) but they come at considerably higher cost. From perspective of lesion creation, spherical inserts similar to acrylic spheres were 3D printed using both FDM, SLA (28). While this approach showed a reduction in the wall effect, it is not completely eliminated. Few studies provided some advancements in creating heterogeneous lesion inserts (34). By producing several small fillable compartments within segmented lesions better intricate radiotracer uptake patterns were seen. While this is a significant improvement in phantom design, one major practical hurdle remains: Filling of these multiple small compartments. In a few other studies, radioactive lesions were created via 3D printing by directly mixing radiotracer into the resin (18,25,26,31) and embedding printed inserts within phantoms. Though the findings are promising, this requires shielded environment with specific ambient conditions. Another limitation is the suitability only for long half-life tracers or high doses of activity concentration for short half-life tracers accounting in the print and acquisition times. A more practical approach involved using 3D-printed fillable grids that better mimic specific tissue distributions and organ structures (22,29,35,36) analogous to certain practices in radiology. The grid's design parameters can be adjusted to simulate different tissue densities thus different attenuations. They also simplify the ability to model complex activity distributions with a single radiotracer injection, as the internal grid structure modulates concentration across various regions, eliminating the need to fill multiple compartments thus minimizing potential errors from using multiple radiotracer solutions with varying activity concentrations. Additionally, the design parameters can be adjusted to considerably lower than the spatial resolution values as mentioned by (29) due to which cold walls within the regions of interest

NOTE: This preprint reports new research that is not certified by peer review and should not be used to guide clinical practice.

inside the grid are avoided. SLA grids of multiple contrasts were studied for nuclear imaging (29,35). Monte Carlo Simulations were also used in complementing validation of such studies proving the compatibility with existing practices.

A key concern for the choice of printing is the radiological properties i.e. water equivalent density and x-ray attenuation (4,11). While SLA printing offered high precision and good quality of the surface, mostly resulting from the properties of the resin, the densities of phantoms are typically higher than water (29). FDM uses materials such as thermoplastics like Poly Lactic Acid (PLA) or ABS which tend to be closer to the desired range (35) hence making them more radiologically compatible for fused imaging applications. In particular, majorly SLA has been explored for grid-based approaches with limited knowledge about FDM's performance in such applications. Also, these grid-based approaches have been focused on SPECT imaging with very little emphasis on PET applications which is reflected on the contrast ratios achieved in these studies compared to current PET detection performance. Unfortunately, most previous designs have been optimized for SPECT or PET, with little consideration given to the dual-modality nature of the imaging in practice (PET/CT and SPECT/CT). Though previous studies have confirmed that the CT based PET attenuation correction works for such studies, water neutral attenuation would be more ideal (22,29,35). Therefore, a standardized approach is needed that accounts for both imaging modalities, leading to a grid design that delivers reliable results in both PET and CT.

We report an investigation of FDM grid-based phantom inserts for PET/CT imaging. Grid spacing, solidity, and different target sizes were investigated as design parameters to balance the trade-off between PET performances without compromising CT attenuation. This work presents, a quantitative study of multiple target detectability and quantitation in 3D-printed grid phantoms for PET/CT imaging. We also report data analysis standards which could aid in more adaptability.

NOTE: This preprint reports new research that is not certified by peer review and should not be used to guide clinical practice.

2. Materials & Methods

2.1. Design and Fabrication of Cubic Grids:

Cubic grids of 4 x 4 x 4 cm were created in Fusion 360 (*Autodesk Inc, San Francisco, SC, USA*) with the Volumetric Lattice toolset. 4 cm size was chosen to accommodate the smallest to largest lesions used in conventional QC practices (12). Two essential design characteristics were incorporated; *Solidity (S)* and *Pore Distance (D_P)*. Solidity (S) is the percentage of solid material that regulates the fillable volume, influencing contrast against the background or target, while Pore Distance (D_P) is the distance between two consecutive pores a.k.a base unit cell which dictates the permeability (*Ease of filling by allowing optimal fluid movement*) and resolution. A key design challenge for the grid is to balance and achieve a suitable trade-off that enhances activity dispersion and movement of air bubbles from the mesh. Three S configurations (50, 60, and 70%) and three D_P variants (5,7,10 mm) were investigated as shown in (**Figure. 1.a**). The target voids of varying diameters (*T*: 10, 15, and 20 mm) were created by a Boolean subtraction centred on the cubic grids (**Figure. 1.b**) and spherical shape was chosen based on conventional QC practices. To streamline the design identification, *S-D_P-T* nomenclature (representing Solidity, Distance, and Target Diameter) was used directly compatible with Fusion 360 over a previously used Fillable Volume Fraction (FVF) by (29). A total of 36 cubes of which a quarter non-target homogenous cubes and the other cubes with spherical targets based on the possible permutations of the *S-D_P-T* were designed for this purpose. Additionally, a cube holder support (Φ 20 cm, 7mm) with a 3 x 3 layout for cube insertion was also designed close to the internal diameter of the NEMA Jaszczak Phantom as in (**Figure. 1.c**) to restrict the movement of cubes inside the phantom. This support structure was also meshed with specifications of *S: 50, D_p: 7 mm,* allowing for efficient mixing of the radioactive tracer activity and enabling air bubbles to move freely. Gyroid pattern belonging to TMPS (Triply Minimal Periodic Structures) family were found to have good directional fluid permeability compared to other patterns (37). After confirmation of homogeneity through some internal tests, gyroid pattern was used for the grid

NOTE: This preprint reports new research that is not certified by peer review and should not be used to guide clinical practice.

structure. The models after meshing were exported as .STL files with minimum resolution of 0.45 mm and were sliced for printing in Prusa Slicer (Prusa Research, Prague, Czech Republic). Each set was then 3D printed with the Prusa MK3S+ Printer (Prusa Research, Prague, Czech Republic) using ABS. ABS is the closest material to emulate water (22), which is typically used in QC procedures, both in terms of physical and radiological properties. The print parameters used can be found in **Table 1**. To characterize the printing accuracy, theoretical calculations of the expected weight for homogenous cubes based on 100% solidity cube were carried out. Printed density (ρ) was also calculated from measured weight and design volume (From Fusion 360). 5% maximum deviation was deemed as acceptable threshold for both weight and density.

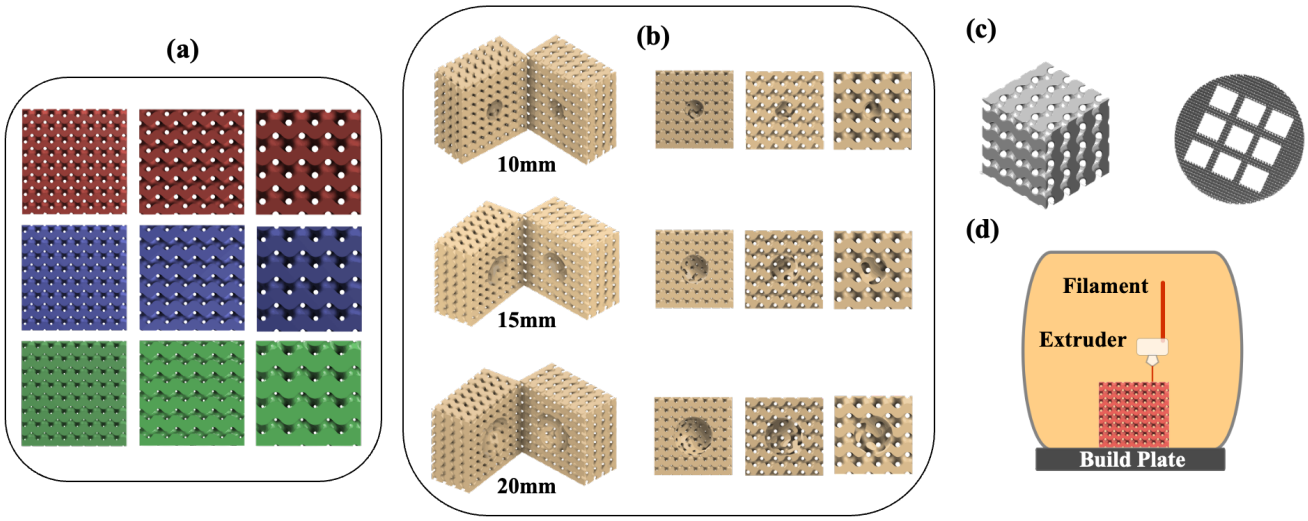

Figure 1. Schematic of Grid Design and Fabrication: (**a**) Central Section of baseline 6 design parameters Rows - S: 50% (Red), 60% (Blue), 70% (Green) & Columns – D_P: 5 mm, 7 mm, 10 mm; (**b**) Split cubes and Central Slice for varying D_P, showing different targets (T: 10 mm, 15mm, 20 mm). (**c**) Rendering of Cube Insert and Designed NEMA Jaszczak Cube Holder used for G-code Generation; (**d**) FDM illustration for fabrication of the designed inserts

NOTE: This preprint reports new research that is not certified by peer review and should not be used to guide clinical practice.

Table 1. Print Parameters for the Cubes	
Filament	ABS Plus (eSUN, Shenzen, China)
Infill	100%*
Print Time	3h (For Each Cube), 7h (For Each Support)
Nozzle Temperature	250 ºC
Bed Temperature	Cubes - 100 ºC
Density	1.01 g/cc
Support	None
*** 100% infill was utilized since the .STL files were already meshed in Fusion 360**	

2.2. Phantom Preparation Protocol – 36 Cube Investigation:

Cubes were positioned within a cylindrical NEMA Jaszczak Phantom as previously mentioned. 36 cubes were arranged in 4 different layers with the exact layer configurations presented in **Figure A1**. The expected Contrast ratio (Between the Cube and Background Water) or Target to background ratio (Between the spherical void and cube) for S: 50, 60, 70 is 2, 2.5, 3.3, which are much higher than previous SPECT studies (27,29,35). However, the exact ratio practically provided by the 3D-printed grid after accounting in printing and imaging artefacts can vary. The simplified phantom preparation protocol is illustrated in **Figure 2**. Phantom Filling is facilitated by a mixture of distilled water and soap, which was used to reduce the liquid's surface tension (38). The phantom was left for 6 hours with this soap solution to allow trapped air bubbles inside the grids to reach the top and dissolve. The phantom was filled with water (**Figure 2 a-c**) on Thursday (*Day 0*) for the initial acquisition, followed by Friday (*Day 1*). It was left undisturbed over the weekend and subsequently used for three additional consecutive acquisitions from Monday to Wednesday (*Day 4-6*), totalling five acquisitions. 20 - 40 minutes before acquisition, tracer is injected into the phantom. Tracer was administered in a single

NOTE: This preprint reports new research that is not certified by peer review and should not be used to guide clinical practice.

injection protocol closer to clinics rather than prediluted stock solution strategy used for similar studies (**Figure 2 d-f**). The tracer used in this study is [^{18}F] FDG (Fluorodeoxyglucose), due to regular clinical usage and was injected on each acquisition day as per **Table 2**.

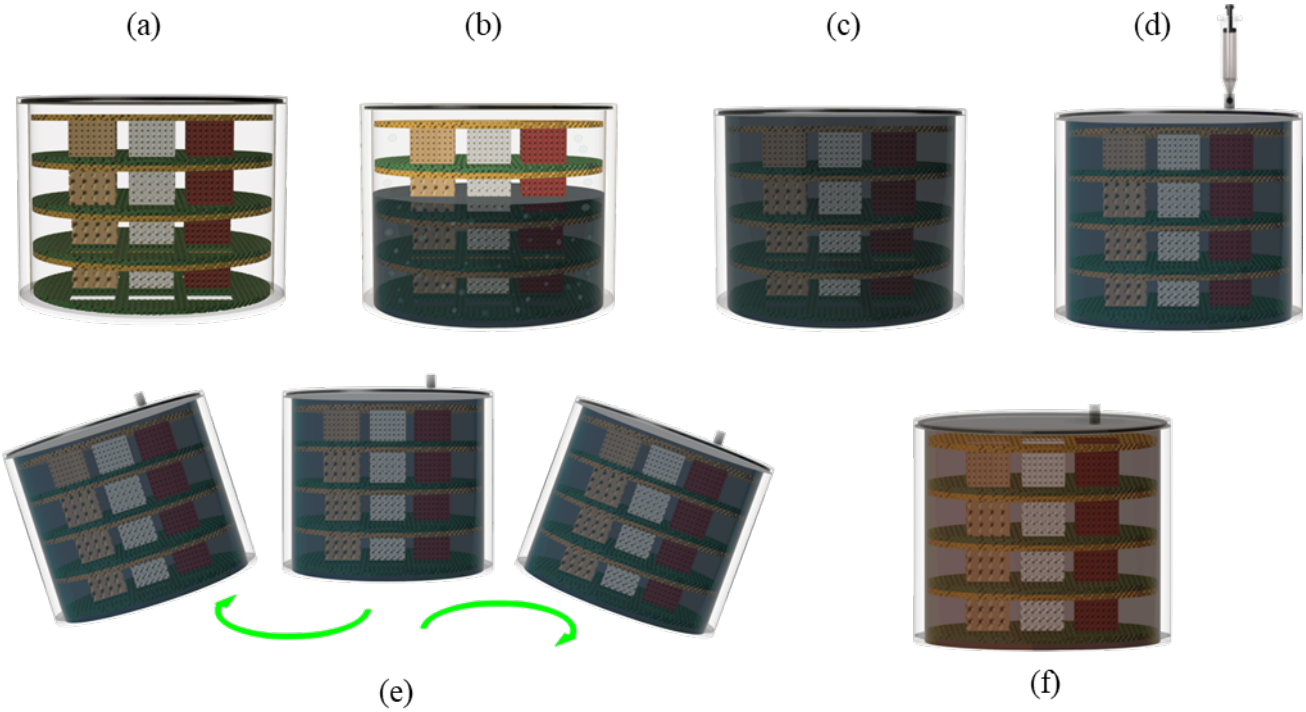

Figure 2. Phantom Preparation Protocol: (**a**) Placement of Support & Cubes inside the Phantom, (**b**) Filling Phantom with Soap Water Solution, (**c**) Phantom Relaxation, (**d**) Injection of Activity, (**e**) Mixing Post-Injection by Shaking, (**f**) Radioactive Phantom Ready for Imaging

Table 2. Injected Activity for Different Acquisitions

Acquisition Number	Injected Activity (MBq/kg)	Decay Time (min)	Activity Concentration at First Acquisition (MBq)	Day
1	82.8	60	56.1	0
2	66	73	41.2	1
3	64.3	45	47.5	4
4	60.4	30	47.5	5
5	54.4	25	45.4	6

NOTE: This preprint reports new research that is not certified by peer review and should not be used to guide clinical practice.

2.3. Imaging & Reconstruction Parameters:

All acquisitions were performed on a Discovery MI 5-ring digital PET-CT system (General Electric Healthcare, Chicago, IL, USA) (39). In the CT component, images were acquired with a slice thickness of 2.8 mm for CTAC, 2.5mm for CT & 1.25mm for High resolution CT. For each experimental iteration, 5 consecutive acquisitions of 5 minutes each centred on the phantom were performed. Applied corrections and protocol were similar to that of a clinical setting. Some acquisition parameters used are summarized in **Table 3**.

Table 3. Acquisition Parameters used for the PET	
Matrix Size	256 x 256
Slice Thickness	2.8mm
No. of Slices	89
Scan Time	300/300/300/300/300 s
Reconstruction Diameter	600 cm
Pixel Dimensions	[2.34 2.34] mm
Voxel Dimensions	2.34 x 2.34 x 2.8 mm
Voxel Volume	15.43 mm^3
Reconstruction Algorithm	QCFX
Beta	550

2.4. Data Extraction and Analysis:

For data assessment, visual comparison of the central axial slices for each cube layer was performed for both CT and PET scans, leading to qualitative proof of concept. The key features observed are the visual changes in the texture of the cubes over time, contrast across features and the visibility of the targets. Subsequently, quantitative data extraction was carried out using image interpretation software PETVCAR on AWServer client console (*General Electric Healthcare, Chicagio, IL, USA*) following the workflow of (12). The three main regions in the DICOM images were classified as Background Water, Cube Mesh, and Targets. For each set of images, 36 spherical VOIs corresponding to the true internal volume of the spheres were placed centered on the cubes (For the non – target cubes, VOI size is maintained same as 20mm target cubes). Additionally, 4 spherical VOIs were placed for each layer

NOTE: This preprint reports new research that is not certified by peer review and should not be used to guide clinical practice.

in background adjacent to the cubes and were averaged per layer. Alongside Hounsfield Units (HU) for the CT and Activity Concentration (kBq/ml) for mean, maximum and standard deviation were extracted. The data extraction led to 1180 measurement values of which 180 HU (*36 cubes across 5 Days)* are from the CT and 1000 Activity concentration (900: *36 cubes across 5 Days with 5 per day* and 100: *4 backgrounds across 5 Days with 5 per day*) from the PET. For each day, HU data was averaged in 2 different sets first as function of solidity and second as function of pore distance. The extracted PET data for each day was averaged over corresponding 5 consecutive acquisitions thus leading to 180 insert VOI values (*36 cubes x 5 days*) and 20 Background values (*4 Layers x 5 Days*).

The SUV was then calculated as below with a phantom weight of 4.5kg,

$$\mathrm{SUV}_{(\mathrm{mean\ /\ max})} = \frac{\text{Extracted Activity Inside ROI in } \frac{\mathrm{Bq}}{\mathrm{ml}} \text{ (Mean/Max)}}{\text{(Injected Activity in Bq)/(Weight of Phantom in g)}} \quad (1)$$

To enable analysis two quantitative metrics were calculated from the SUV data namely the Recovery Coefficient (RC) and Dilution Coefficient (DC). Both mean and maximum for these metrics were calculated using equations 2 & 3.

- Recovery Coefficient (RC) representing the dispersion of activity within the target voids relative to the Background Water (12).

$$\mathrm{RC}_{(\mathrm{mean/max})} = \frac{\text{SUV Inside the Target (Mean/Max)}}{\text{SUV in the Background Water (Mean/Max)}} \quad (2)$$

- Dilution Coefficient (DC) represents the contrast between the printed homogenous cube and the Background Water. This is analogous to contrast modulation coefficient in (29) and is only used for non-target cubes

$$\mathrm{DC}_{(\mathrm{mean/max})} = \frac{\text{SUV Inside the Homogenous Cube (Mean/Max)}}{\text{SUV in the Background Water (Mean/Max)}} \quad (3)$$

NOTE: This preprint reports new research that is not certified by peer review and should not be used to guide clinical practice.

Theoretical DCs are 0.5, 0.4, and 0.3, corresponding to Contrast / TBR of 2, 2.5, and 3.33, respectively. To assess the homogeneity in background activity concentration, SUV values across 4 layers for each day were analyzed and a pairwise errors across layers were calculated. An acceptable threshold of 10% similar to QC uniformity studies (11) was chosen. A subsequent statistical analysis on the combined dataset of 180 PET metrics (RC + DC) was performed for normality through the Shapiro-Wilk (40) separately on both median and maximal values. The normality tests were complemented by a non-parametric counterpart, Friedman Test to assess global consistency across the metrics over 5 days (41). Post Hoc of Wilcoxon signed-rank test with Bonferroni correction (9,42) was performed to investigate the pairwise statistical differences between days. All statistical analyses were conducted with a predetermined significance level of $p < 0.05$.

3. Results:

3.1. Assessment of Printing Accuracy

The 3D printed cubes had high accuracy in the aspect of weight, with all measurements within 5% of expected. The weight measurements of the cubes on the print day can be found in **Table 4**. The highest deviation of 3.125%, was observed for the 50-10-0 & 50-7-0 cubes. The density of the printed section of the grids was estimated to be between 0.97 – 1.03 g/cc, which is close to water with reference value of 1 g/cc. **Figure 3** illustrates the printing of the cubes, also the results post printing for one of the layers.

NOTE: This preprint reports new research that is not certified by peer review and should not be used to guide clinical practice.

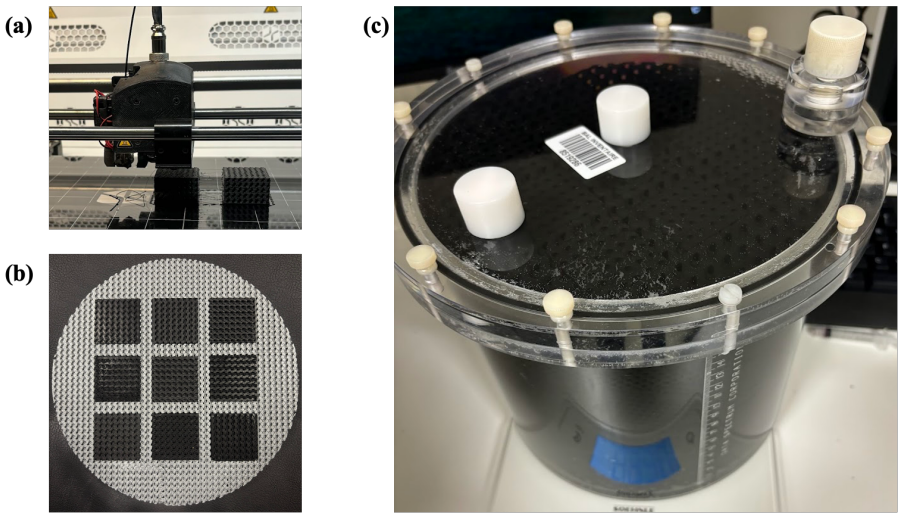

Figure 3. (a) Snapshot of Cubes while Printing; (b) Printed inserts arranged in 3x3 layout using the Cube Holder; (c) Assembled NEMA Jaszczak Phantom post filling

Table 4. Measured Weight of 3D Printed Cubes

Cube (S-D-T)	Measured Weight (g)	Expected Weight (g)	Difference in Weight (%)	Effective Density (g/cc)
100-0-0	64	-	-	-
50-5-0	32	32	0	1.00
50-7-0	33	32	-3.125	1.03
50-10-0	31	32	3.125	0.97
60-5-0	37.5	38.4	2.34	0.98
60-7-0	37.3	38.4	2.86	0.97
60-10-0	38	38.4	1.04	0.99
70-5-0	44	44.8	1.79	0.98
70-7-0	44	44.8	1.79	0.98
70-10-0	44.1	44.8	1.56	0.98

NOTE: This preprint reports new research that is not certified by peer review and should not be used to guide clinical practice.

3.2. CT Progression over 5 days:

CT image assessment showed a clear temporal trend among Hounsfield Unit (HU) values. Qualitative visualization of images, viewed at the same intensity windowing (*W: -40, L: 400; Abdominal Windowing*), showed a visual improvement in rendering with prolonged immersion of cubes as shown in **Figure 4.a**. The minimum HU value within the VOI's was -40 ± 6 (Day 0) and maximum value observed -9 ± 4 (Day 5). HU values varied across the cubes, but mean HU values had a trend toward neutral attenuation of HU ~ 0 (water) with reduced standard deviations across the days. This trend is illustrated in **Table 5** & **Figure.4b, 4c** for the homogenous cubes. The HU reduced at an average 10-15% per immersion day irrespective of design parameter. Pore distance (D_P) of 5mm exhibited the most drastic variation in HU values proportion to spatial resolution on the image throughout the five-day regimen as seen in **Figure 4.a**.

Table 5. Hounsfield Units values for Homogenous Cubes

Solidity (%)	Pore Distance (mm)	Hounsfield Units (Mean ± *SD*)				
		Day 0	Day 1	Day 4	Day 5	Day 6
50	5	-21.4±4.9	-16.6±3.7	-9.8±3.5	-6.4±3.2	-4.4±3.7
	7	-21.5±5.2	-19.3±4.2	-12.9±4.1	-11.6±3.9	-12.1±3.3
	10	-20.5±11.8	-21.1±10	-15.1±8.3	-13.7±7.6	-12.9±6.6
60	5	-21.9±3.5	-19.2±3.4	-12.3±3.2	-8.9±3.8	-8.7±3.7
	7	-34.5±9.2	-22.7±9.1	-19.5±9.2	-21.6±7.8	-17.5±8.1
	10	-26.1±11.6	-25.2±11.2	-17.6±8.8	-10.8±7.4	-15.2±7.6
70	5	-28.4±4.9	-25.2±3.9	-18.3±4.3	-15.9±4.3	-14.4±3.5
	7	-39.9±5.7	-37.8±5.5	-29.8±5.9	-27.9±4.9	-27.8±4.8
	10	-31.2±7.9	-26.5±8.0	-23.2±8.2	-20.0±8.0	-20.6±7.4

NOTE: This preprint reports new research that is not certified by peer review and should not be used to guide clinical practice.

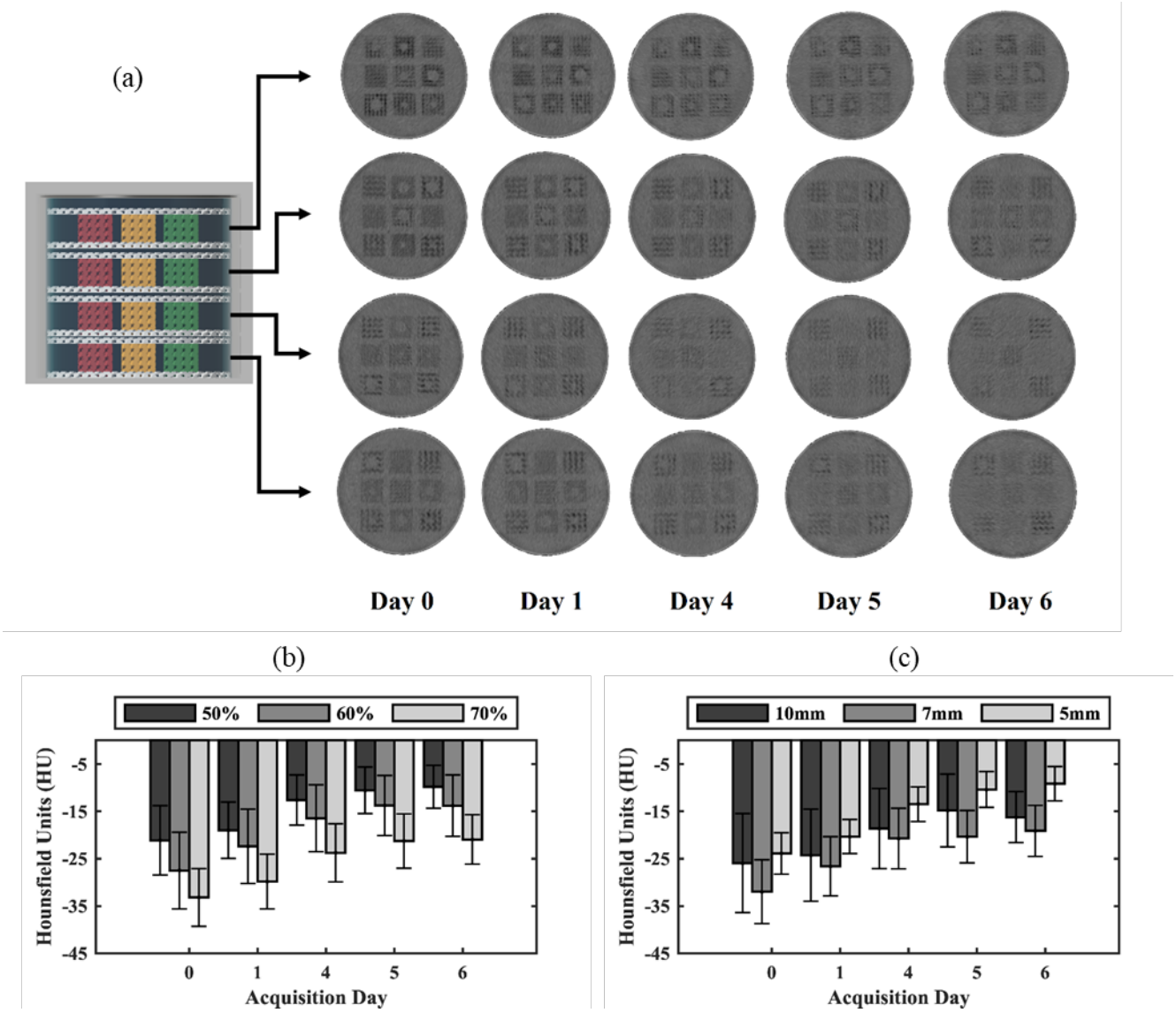

Figure 4. (a) CT progression of Central Axial Slice over 5 Acquisition Days viewed on Abdominal Windowing *(-160 to 240)*; (b) Averaged HU values as function of Pore Distance (D_P) & Acquisition Day; (c) Averaged HU values as function of Solidity (S) for Homogenous Cubes & Acquisition Day – Error bars indicate Standard Deviation

3.3. PET Uptake Across Five Days:

Contrast differences in the PET images viewed on the same SUV window (*0-2 g/ml*) are illustrated in **Figure 5.a**. Visual inspection of the images shows clear demarcation among contrasts between the printed cubes, target voids, and the background water. The targets are all distinguishable, but visibility

NOTE: This preprint reports new research that is not certified by peer review and should not be used to guide clinical practice.

reduces as the size decreases. The 70% solidity cubes are the most distinct, and the 50% solidity cubes are the least distinct in terms of visual contrast. Another difference observed is between different layers of the phantom, the activity concentration in the background water is not uniform consistently. Ideally, this should not affect the indicators since they are based on local normalization for each layer. No significant differences apart from this can be seen between days. Dilution Coefficient values for the 9 homogenous cubes are presented in **Figure 5.b**. Dilution coefficients expected for respective solidities are 0.5, 0.4, and 0.3. For 50% solidity, the dilution coefficients fluctuate around the theoretical value of 0.5, with extreme outliers based on the pore distance and days. For 60% solidity, the coefficients of dilution range from 0.35 to 0.48, showing consistent deviation. 70% solidity, the coefficients of dilution are consistently higher than the expected 0.3, with values ranging from 0.32 to 0.40. Recovery Coefficient (RC) mean and maximum values are presented in **Figure 6**. Recovery Coefficient values had variability over the five acquisition days for all three pore distances 5mm, 7mm, and 10mm but no clear quantitative pattern was seen as function of acquisition day unlike the CT HU values. The larger spherical targets (20mm) consistently demonstrated RC values to ideal expectations which dropped significantly for 10mm targets. The quantitative variability in background SUV_{Mean} and SUV_{Max} are presented on **Figure 7.a, 7.b.**

Table 6. Summary of Statistical Tests

Statistical Test	Key Results (Significance – 0.05)
Shapiro-Wilk Normality Test	DC_{Max} + RC_{Max}: W = 0.91, *p-value* <0.001 DC_{Mean} + RC_{Mean}: W = 0.93, *p-value* <0.001
Friedman Test	DC_{Max} + RC_{Max}: *p-value* = 0.9755 DC_{Mean} + RC_{Mean}: *p-value* = 0.9323

NOTE: This preprint reports new research that is not certified by peer review and should not be used to guide clinical practice.

The results of statistical tests can be found in **Table 6** and **Figure 7.c, 7.d**. All the data was fund to be non – normal based on Shapiro wilk. Friedman tests show that the deviation in normalized values are not statistically significant across days. Wilcoxon Tests though suggest that for combinations with Day-4 for the maximum and Day-6 and Day-4 for the mean measurements are statistically distinct.

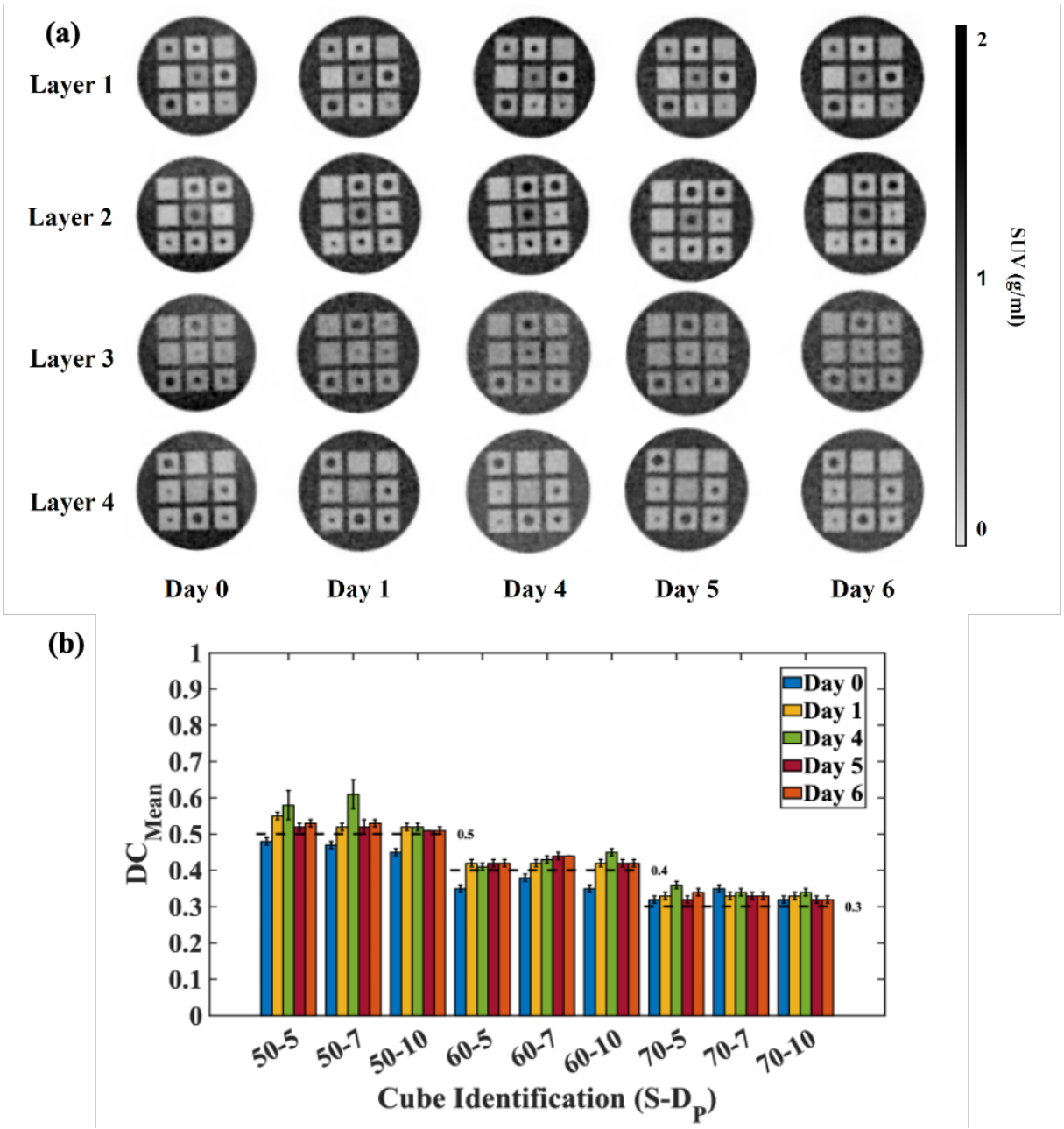

Figure 5. (a) Central Axial PET Slice for each layer over 5 Acquisition Days viewed on Same SUV Window Scale; (b) DC_{Mean} values as function of Pore Distance – Error bars indicate Standard Deviation (SD) *(Corresponding DC_{Mean} & DC_{Max} data can be found in Table A1)*

NOTE: This preprint reports new research that is not certified by peer review and should not be used to guide clinical practice.

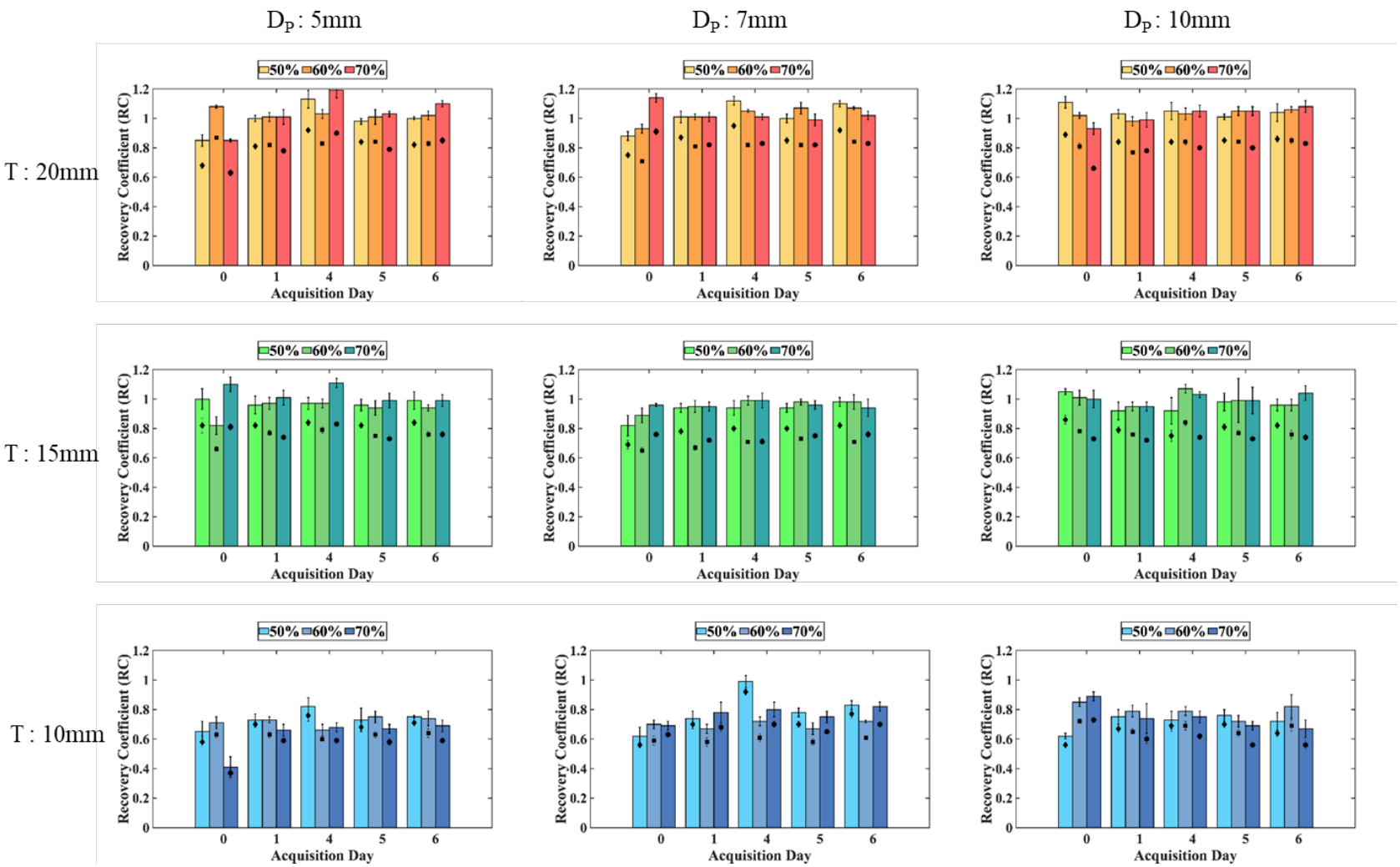

Figure 6. Recovery Coefficient Bar Plots for 36 Cube study as Function of Solidity (S) and Pore Distance (D_P) over different acquisition days; The Bars represent RC_{Max} with error bars (SD) and the filled markers inside the bar plots represent corresponding RC_{Mean}. Figure is arranged as Rows (Targets : 20, 15, 10mm) & Columns (Pore Distance : 5, 7, 10mm). *(Corresponding Data can be found in Tables A2, A3 & A4)*

NOTE: This preprint reports new research that is not certified by peer review and should not be used to guide clinical practice.

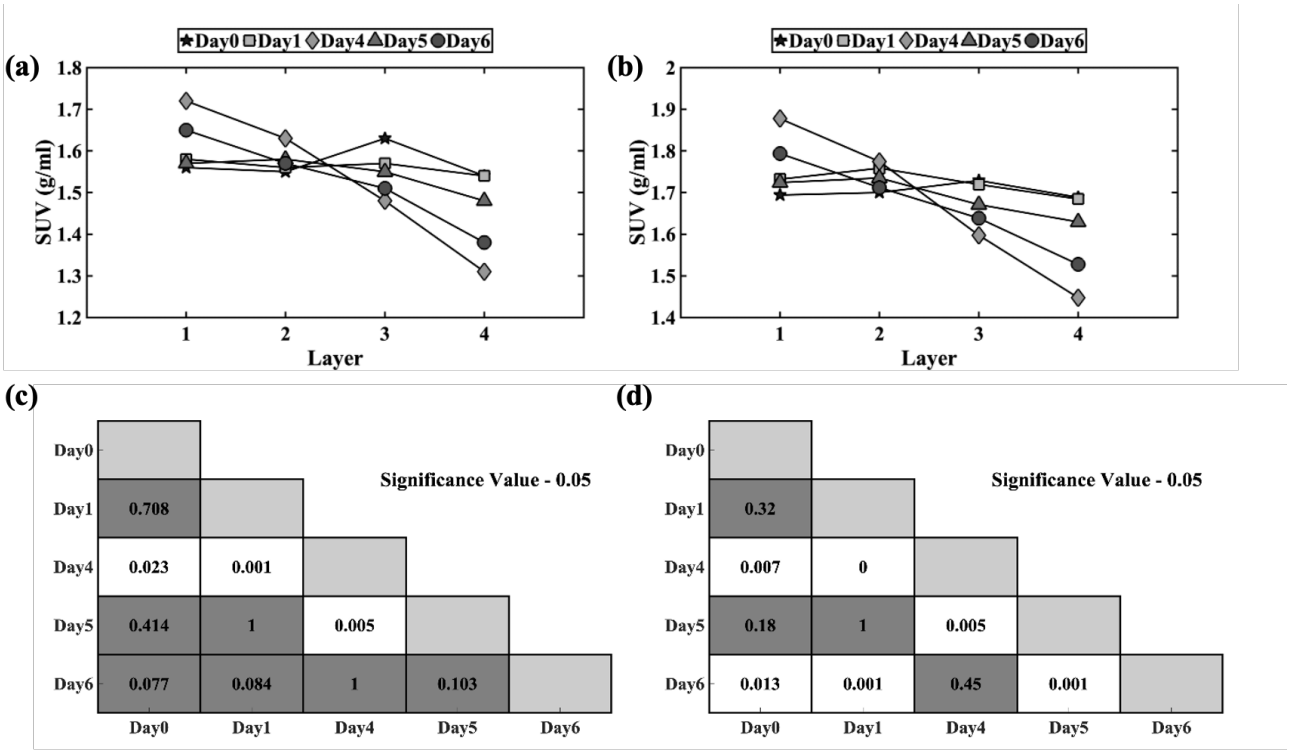

Figure 7. SUV variation across 4 layers (a) SUV_{Mean} (b) SUV_{Max}; Wilcoxon signed-rank test with Bonferroni correction $p - value$ matrix for (c) RC_{Max} + DC_{Max} and (d) RC_{Mean} + DC_{Mean} - White represents combinations that have statistical differences

4. Discussion:

Low Cost FDM based 3D printed cubic inserts were explored as possible alternative to acrylic sphere to create targets in PET/CT QC phantoms. 36 cubic inserts of which 27 with spherical targets were considered. A new protocol of single injection with a buffer diffusion time was utilized. Qualitative CT and PET images were analyzed, quantitatively HU values for CT and 2 metrics - RC and DC for PET were studied. Statistical differences across days globally were looked upon following up with pairwise comparison across days.

Printing accuracy of the cubes weighing between ± 5% of expectation indicates the accuracy of FDM in the production of phantom inserts with precision which is crucial for true representation of the planned experimental setup. These also fall within the prescribed thresholds of previous 3D printing-based studies (29,35). The equivalent density of the solid component (0.97 – 1.03 g/cc) fall within the

NOTE: This preprint reports new research that is not certified by peer review and should not be used to guide clinical practice.

range of water which is a beneficial property for neutral attenuation. It should be noted that reproducibility of FDM can be subject to various factors, such as material behavior, print conditions and design complexity. One such design limitation in this study was the Pore Distance which had to be limited to 5mm considering the printers resolution.

From the PET/CT, the temporal pattern shift observed in Hounsfield Unit (HU) measurements on the CT over the course of the seven-day immersion period strongly suggests a dynamic interaction between the ABS material and the surrounding water environment. Qualitative and Quantitative enhancement in the image rendering observed confirms the exploitation of the printing inaccuracies of FDM. The water molecules, as they fill up the available air spaces due to printing defects cause a rise in the bulk density of the material itself during the scan (43,44). Additionally, this very process could also be responsible for causing a reallocation of the electron density in the material contributing to change in HU values. Hence, Temporal CT attenuation changes necessitate special attention to the history of immersion for 3D printed phantom inserts.

PET images presented a contrast picture with no appreciable qualitative or quantitative evidence for the same phenomenon. A plausible explanation is that the injection of the radiotracer performed every acquisition day prior to scanning, limits the time window during which there may be significant material changes to manifest in the PET data. For a full exploration of the effect on PET, future studies using radiotracers with longer half-lives than in this work are recommended. One of the parameters which is not explicitly mentioned in this work is the pore size which reduces in proportion with pore distance. Lower pore distances within same solidity can lead to pore sizes lower than the resolution of both CT and PET making them qualitatively invisible on the images (29). A limitation in this regard is that a threshold for D_P balancing fluid permeability, spatial resolution and quantitative performance is yet be identified. Thus, a future dataset optimization on D_P can enable anthropomorphic studies like (29,35) with FDM to reduce the gap from clinical reality. Evident visible contrast variations in the PET images verified that the scanner could indeed distinguish three regions among the printed cubes, target

NOTE: This preprint reports new research that is not certified by peer review and should not be used to guide clinical practice.

voids, and background water which is essential for the accurate quantification of radiotracer uptake. The fact that 70% solidity cubes had the maximum visual contrast, whereas 50% solidity cubes had the minimum visible contrast, highlights the increased solidity causes a more uniform averaging of activity within the cubes, resulting in better contrast. Visually, as the target size reduces the visibility reaches closer to the systems limitation as mentioned by (12). Quantitative metrics show a comparable recovery coefficient to that of walled spheres of similar ratios (9). Recovery coefficients were consistent across days and no significant statistical differences were observed globally supported by the *p*-values of Freidman tests (**Table 7**). The recovery coefficients also highlighted the complexity of tracer distribution and quantification in FDM-printed inserts. For D_P: 5mm, 69% of RC_{Max} values and 39% of RC_{Mean} values yielded greater than 80% recovery. 62% of the RC_{Max} values and 32% of the RC_{Mean} values exceeded same threshold for D_P: 7mm and for D_P: 10mm, the distribution observed was 65% for RC_{Max} and 36% for the RC_{Mean}. This indicates that the proportions of RC_{Max} and RC_{Mean} values greater than 0.8 (45) were consistent for all D_P conditions, implying that the pore distance, within the range tested, did not have a significant influence on the overall tracer recovery. This is in line with previous studies (29), the fillable volume fraction / solidity of the printed inserts is the key factor driving PET performance. The practically achieved contrast averaged on all data as function of solidity were 1.93 ± 0.14, 2.44 ± 0.2 & 3.01 ± 0.08 against theoretical contrast of 2, 2.5 and 3.33. Additionally, individual DC_{Mean} and DC_{Max} (**Figure 5b, Table A1**) indicated a slight systematic bias in practical contrast achieved compared to theoretical values. Hence though globally, the achieved contrast is within the thresholds but the precise value for every experiment can vary in agreement with similar studies (29,35).

The proposed protocol in this study injects activity in a prefilled phantom rather than a stock prediluted strategy used previously by (27). This was specifically designed to follow the evolution of CT in conjunction with PET repeatability on multiple days. Another consideration included as mentioned in previous studies (27,29) is sensitivity to air bubbles. The proposed protocol due to its increased

NOTE: This preprint reports new research that is not certified by peer review and should not be used to guide clinical practice.

immersion strategy had no air bubbles at the scan resolutions as seen in the extracted HU values (**Table. 5**) as well. But this opens the phantom to diffusion discrepancies causing SUV distribution variability along the phantom. In fact, non-uniformity of the activity dispersion in background across phantom layers was apparent as seen in **Figure 6**. The layer variation for Day-4 and Day-6 values fail the 10% threshold as seen in **Figure A2, A3.** It is also to be noted that injected activity and initial decay time **Table 2** were not the same for various days hence normalization was performed. While local normalization reduced these discrepancies as seen in global *p* values of Friedman, significance of SUV variation on the metrics is highlighted by the pairwise *p* value maps from Wilcoxon test observed in **Figure 7** where the *p* value decreases significantly for combinations with Day – 6 and Day – 4. This discrepancy indicates a potential bias between grid attained contrast compared to theoretical value. To address this comprehensively, a robust preparation protocol and a larger 3D printed dataset as mentioned previously are necessary with more design parameters correlated with achievable contrast ratios vs theoretical. This enables calibration, offsetting printing inaccuracies, non-homogeneity and finally the tracer in use. For future studies, possibly EARL protocol – removing volume (Example 10ml) of the phantom (distant from the targets) unfilled during the phantom shaking step and adding it back prior to scan could be utilized (4,11,46) to reduce this potential bias.

The biggest finding in this study is that 36 targets can be analyzed at once rather than 6 fixed targets in a conventional experimental setup. In terms of impact, this can be reflected as 6 times lower experiments for same target sizes at the minimum and significant amount of radiation exposure reduction. This number can be further reduced or increased depending on the target sizes of interest. Another goal of this study was also to demonstrate the wall-less effect compared to acrylic spheres. When looked at carefully, the SUV profile of select cubes from Day 1 and Day 5; (70-5) shown in **Figure A4** comparable to that of profiles from (9). We see a flat line as expected for non-target cubes, a peak whose width and height varies with target size for targeted cubes. Since the phantom has 3 different regions as mentioned previously leading to 2 regional transitions, this can be clearly observed

NOTE: This preprint reports new research that is not certified by peer review and should not be used to guide clinical practice.

on the SUV profile where target to cube is observed followed by cube to water. A key limitation though of this study is the manual data extraction using actual physical volume of the target as the VOI volume leading to profound spillovers thus underestimation. While this extraction method worked for walled spheres previously (12), due to no explicitly distinguishable wall neither on CT nor PET it becomes difficult to accurately delineate the targets for printed cubes. Sensitivity to manual errors also increase compared due to increased No. of targets - 36. This is one of the reasons why targets contrast with respect to its native cube background were not included in this study. Hence, a more consistent automatic extraction method accounting in the printing inaccuracies and spill out is necessary for robust data and TBR analysis in future studies. Further, to perform any such multi acquisition – comparison studies, the combination of effective activity at scan and pairwise layer variability is more important than pairwise statistical *p* values. For, instance Day-4 vs Day-6 might yield the same *p* value as Day-1 vs Day-5 (**Figure. 7c, 7d)**, but the former can be ruled out because of layer variability criteria. Furthermore, comparisons with Day-0 can be ruled out entirely because of effective activity at scan criteria (**Table. 2**). Therefore, through such multi-criteria standards, we can ensure conclusions that are both statistically and practically meaningful.

Beyond these points, dimensional inaccuracies resulting from material shrinkage and warping during printing especially for ABS make the standardization challenging across printers. Also, printing ABS demands for an enclosure to avoid harmful toxicity which reduces usage in hospitals. While equally priced to FDM, generic SLA resins are less ideal for dual-modality imaging since they lack the ability to fulfill the needs of CT. It should be noted that alternative new age SLA resins or low density FDM filaments used have potential for greater resolution whilst maintaining neutral attenuation. Though they come at a relatively higher cost, the overall production cost is significantly lower than industrially used polyjet printing (18,26,29). We further comment that the choice of the 3D printed insert design for any such studies must be informed by the main aim: if the concern is only about PET performance, fillable volume (Solidity) optimization is the main priority. However, if enhanced CT performance

NOTE: This preprint reports new research that is not certified by peer review and should not be used to guide clinical practice.

concurrent with PET performance is deemed, then material in use and D_P become the critical design parameters. To expand on this, use of walled spheres without neutral attenuation makes them visible on CT and causes PET edge artefacts. Ideally, to effectively challenge new age PET CT reconstruction algorithms and analysis software's, lesions that are *not explicitly* visible on CT but *only on* PET could be of great advantage. This would enable to study activity concentration changes without anatomical cues from the CT. Furthermore, in this study we reproduced conventional practices but using 3D printing meaning homogenous regions and spherical targets. A larger advantage to advocate for further 3D printing backed grid-based studies is its inherent capability to also create heterogeneity, for example creating a second grid within the target void. Besides, anthropomorphic lesions (33,34), which are directly segmented out of patient scans, can be translated into grid-based insert designs, effectively simulating patient-specific anatomy and activity distributions. D_P becomes equally important along with Solidity as the studies move closer to clinical settings. While this study has identified some of the limitations, such as potential biases due to printing or phantom preparation, the major benefits of grid-based approach far outweigh these limitations. With the development of more comprehensive datasets for a wider range of design parameters and printing conditions, these limitations can be effectively overcome. Therefore, we conclude that FDM based ABS inserts for PET CT produce consistent results which are both reliable and reproducible whilst comparable to that of SLA grids and can be extended for more anthropomorphic studies.

NOTE: This preprint reports new research that is not certified by peer review and should not be used to guide clinical practice.

5. Conclusion:

Feasibility of FDM based 3D printed inserts was established for PET/ CT applications. The quantitative metrics were found to be consistent globally across the acquisitions. A single injection protocol with buffer decay time was used instead of pre diluted stock solution which reduced sensitivity to air bubbles but introduce activity diffusion bias which can be corrected. Further to summarize, the main contributions from this study are as follows

1. Simplified phantom preparation protocol – Reduction in radiation exposure
2. Balancing dual nature of PET/CT
3. Increasing No. of targets scanned per experiment
4. Demonstration Wall free effect
5. Reduced costs of 3D printed inserts

These results open the ground for exploiting FDM based printing for more clinically relevant geometries and activity concentration profiles.

NOTE: This preprint reports new research that is not certified by peer review and should not be used to guide clinical practice.

Abbreviations used in this article are:

ABS	Acrylonitrile Butadiene Styrene
A	Activity Concentration in kBq/ml
DC	Dilution Coefficient
DMI	Discovery MI
D_P	Distance between pores
FDM	Fused Deposition Modelling
FDG	Fluorodeoxyglucose
FOV	Field of View
HU	Hounsfield Units
IEC	International Electrotechnical Commission
NEMA	National Electrical Manufacturing Association
NM	Nuclear Medicine
PET / CT	Positron Emission Tomography / Computed Tomography
PLA	Poly Lactic Acid
QC	Quality Control
RC	Recovery Coefficient
S	Solidity
SD	Standard Deviation
SLA	Stereolithography
SPECT/CT	Single Photon Emission Computed Tomography / Computed Tomography
SUV	Standard Uptake Value
TOF	Time of Flight
TBR	Target to Background Ratio
TMPS	Triply Minimal Periodic Structures
VOI	Volume of Interest

NOTE: This preprint reports new research that is not certified by peer review and should not be used to guide clinical practice.

Appendix

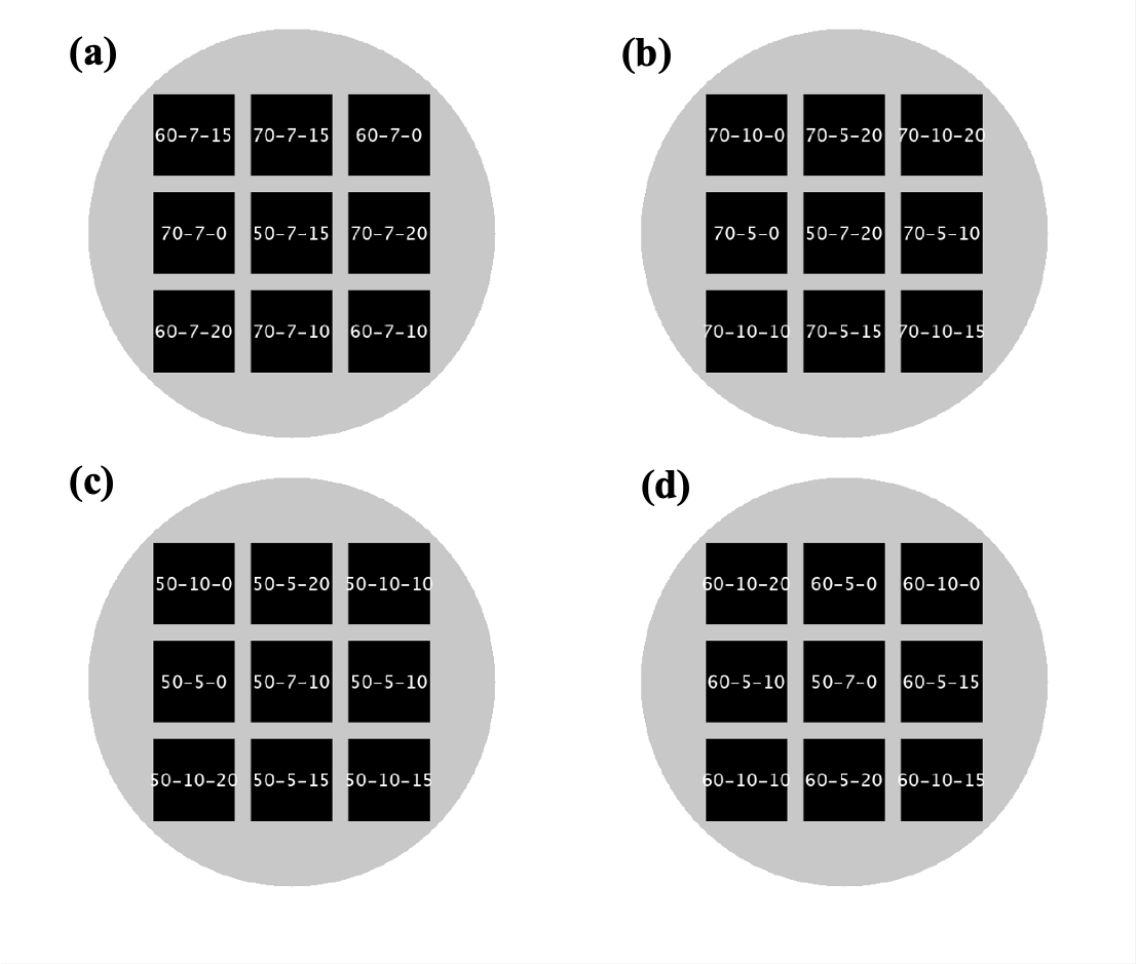

Figure A1. Layout of the 36 Cubes inside the phantom subdivided into 4 Layers – (a) Layer , (b) Layer 2, (c) Layer 3, (d) Layer 4

Table A1. Dilution Coefficient values for Homogenous Cubes

Solidity %	Pore Distance mm	Dilution Coefficient (Max ± *SD* & Mean ± *SD*)				
		Day 0	Day 1	Day 4	Day 5	Day 6
50	5	0.51±0.01 0.48±0.01	0.58±0.01 0.55±0.01	0.64±0.04 0.58±0.01	0.59±0.02 0.52±0.01	0.59±0.00 0.53±0.00
	7	0.49±0.01 0.47±0.01	0.54±0.01 0.52±0.01	0.67±0.04 0.61±0.04	0.54±0.01 0.52±0.02	0.54±0.01 0.53±0.01
	10	0.50±0.01 0.45±0.01	0.56±0.02 0.52±0.01	0.55±0.02 0.52±0.01	0.55±0.02 0.51±0.00	0.53±0.02 0.51±0.01
60	5	0.38±0.02 0.35±0.01	0.45±0.02 0.41±0.01	0.45±0.01 0.41±0.01	0.44±0.01 0.42±0.01	0.44±0.01 0.42±0.01
	7	0.42±0.01 0.38±0.01	0.44±0.01 0.42±0.01	0.44±0.01 0.43±0.01	0.45±0.01 0.44±0.01	0.46±0.02 0.44±0.00
	10	0.38±0.02 0.35±0.01	0.48±0.02 0.42±0.01	0.48±0.02 0.45±0.01	0.44±0.02 0.42±0.01	0.44±0.02 0.42±0.01
70	5	0.34±0.02 0.32±0.01	0.35±0.02 0.33±0.01	0.40±0.02 0.36±0.01	0.34±0.01 0.32±0.01	0.37±0.02 0.34±0.01
	7	0.36±0.01 0.35±0.01	0.36±0.02 0.33±0.01	0.36±0.01 0.34±0.01	0.36±0.02 0.33±0.01	0.36±0.01 0.33±0.01
	10	0.33±0.01 0.32±0.01	0.35±0.01 0.33±0.01	0.38±0.02 0.34±0.01	0.36±0.03 0.32±0.01	0.34±0.01 0.32±0.01

NOTE: This preprint reports new research that is not certified by peer review and should not be used to guide clinical practice.

Table A2. Recovery Coefficient values for Target Cubes (D_P: 5mm)

Solidity %	Target Size mm	Recovery Coefficient (Max ± *SD* & Mean ± *SD*)				
		Day 0	Day 1	Day 4	Day 5	Day 6
50	20	0.85±0.04 0.68±0.02	1.00±0.02 0.82±0.01	1.13±0.06 0.92±0.01	0.98±0.02 0.84±0.01	1.00±0.01 0.82±0.01
	15	1 ± 0.07 0.82±0.05	0.96±0.06 0.82±0.02	0.97±0.04 0.84±0.02	0.96±0.04 0.82±0.01	0.99±0.06 0.84±0.02
	10	0.65±0.07 0.58±0.04	0.73±0.04 0.70±0.02	0.82±0.06 0.76±0.04	0.73±0.08 0.68±0.04	0.75±0.01 0.71±0.01
60	20	1.08±0.01 0.87±0.01	1.01±0.03 0.82±0.01	1.03±0.03 0.83±0.01	1.01±0.05 0.84±0.01	1.02±0.03 0.83±0.02
	15	0.82±0.06 0.66±0.02	0.97±0.04 0.77±0.02	0.97±0.03 0.79±0.02	0.94±0.05 0.75±0.01	0.94±0.02 0.76±0.02
	10	0.71±0.04 0.63±0.02	0.73±0.02 0.63±0.01	0.66±0.04 0.60±0.01	0.75±0.04 0.63±0.02	0.74±0.05 0.64±0.03
70	20	0.85±0.01 0.63±0.02	1.01±0.05 0.78±0.02	1.19±0.05 0.90±0.01	1.03±0.02 0.79±0.01	1.10±0.02 0.85±0.02
	15	1.10±0.05 0.81±0.02	1.01±0.05 0.74±0.01	1.11±0.03 0.83±0.01	0.99±0.05 0.73±0.03	0.99±0.04 0.76±0.02
	10	0.41±0.07 0.37±0.05	0.66±0.04 0.59±0.01	0.68±0.03 0.59±0.01	0.67±0.03 0.58±0.02	0.69±0.04 0.59±0.01

Table A3. Recovery Coefficient values for Target Cubes (D_P: 7 mm)

Solidity %	Target Size mm	Recovery Coefficient (Max ± *SD* & Mean ± *SD*)				
		Day 0	Day 1	Day 4	Day 5	Day 6
50	20	0.88±0.03 0.75±0.01	1.01±0.04 0.87±0.01	1.12±0.03 0.95±0.01	1 ± 0.03 0.85±0.02	1.10±0.02 0.92±0.01
	15	0.82±0.07 0.69±0.03	0.94±0.03 0.78±0.01	0.94±0.05 0.80±0.01	0.94±0.03 0.80±0.01	0.98±0.03 0.82±0.02
	10	0.62±0.06 0.56±0.02	0.74±0.05 0.70±0.03	0.99±0.04 0.92±0.02	0.78±0.03 0.70±0.02	0.83±0.03 0.77±0.03
60	20	0.93±0.03 0.71±0.01	1.01±0.02 0.81±0.01	1.05±0.01 0.82±0.01	1.07±0.04 0.82±0.01	1.07±0.01 0.84±0.01
	15	0.89±0.05 0.65±0.02	0.95±0.04 0.67±0.02	0.99±0.03 0.71±0.00	0.98±0.02 0.73±0.01	0.98±0.05 0.71±0.01
	10	0.70±0.03 0.59±0.01	0.67±0.03 0.58±0.02	0.72±0.03 0.61±0.01	0.67±0.04 0.58±0.02	0.72±0.01 0.61±0.00
70	20	1.14±0.03 0.91±0.02	1.01±0.03 0.82±0.01	1.01±0.02 0.83±0.01	0.99±0.04 0.82±0.01	1.02±0.03 0.83±0.01
	15	0.96±0.01 0.76±0.01	0.95±0.03 0.72±0.01	0.99±0.05 0.71±0.02	0.96±0.03 0.75±0.01	0.94±0.06 0.76±0.02
	10	0.69±0.02 0.63±0.01	0.78±0.01 0.68±0.03	0.80±0.05 0.70±0.02	0.75±0.04 0.65±0.01	0.82±0.03 0.70±0.01

Table A4. Recovery Coefficient values for Target Cubes (D_P: 10mm)

Solidity %	Target Size mm	Recovery Coefficient (Max ± *SD* & Mean± *SD*)				
		Day 0	Day 1	Day 4	Day 5	Day 6
50	20	1.11±0.04 0.89±0.02	1.03±0.03 0.84±0.01	1.05±0.06 0.84±0.01	1.01±0.02 0.85±0.01	1.04±0.06 0.86±0.02
	15	1.05±0.02 0.86±0.03	0.92±0.06 0.79±0.02	0.92±0.09 0.75±0.04	0.98±0.06 0.81±0.02	0.96±0.04 0.82±0.02
	10	0.62±0.02 0.56±0.01	0.75±0.05 0.67±0.03	0.73±0.06 0.69±0.04	0.76±0.04 0.70±0.02	0.72±0.06 0.64±0.02
60	20	1.02±0.02 0.81±0.02	0.98±0.03 0.77±0.01	1.03±0.04 0.84±0.02	1.05±0.03 0.84±0.01	1.06±0.02 0.85±0.02
	15	1.01±0.02 0.78±0.02	0.95±0.06 0.76±0.01	1.07±0.03 0.84±0.02	0.99±0.15 0.77±0.02	0.96±0.04 0.76±0.03
	10	0.85±0.03 0.72±0.02	0.79±0.04 0.65±0.05	0.79±0.03 0.69±0.03	0.72±0.04 0.64±0.02	0.82±0.08 0.69±0.04
70	20	0.93±0.04 0.66±0.02	0.99±0.05 0.78±0.01	1.05±0.04 0.80±0.00	1.05±0.03 0.80±0.01	1.08±0.04 0.83±0.01
	15	1.00±0.06 0.73±0.01	0.95±0.03 0.72±0.01	1.03±0.02 0.74±0.01	0.99±0.09 0.73±0.03	1.04±0.05 0.74±0.02
	10	0.89±0.03 0.73±0.02	0.74±0.09 0.60±0.03	0.75±0.04 0.62±0.02	0.69±0.03 0.56±0.02	0.67±0.06 0.56±0.03

NOTE: This preprint reports new research that is not certified by peer review and should not be used to guide clinical practice.

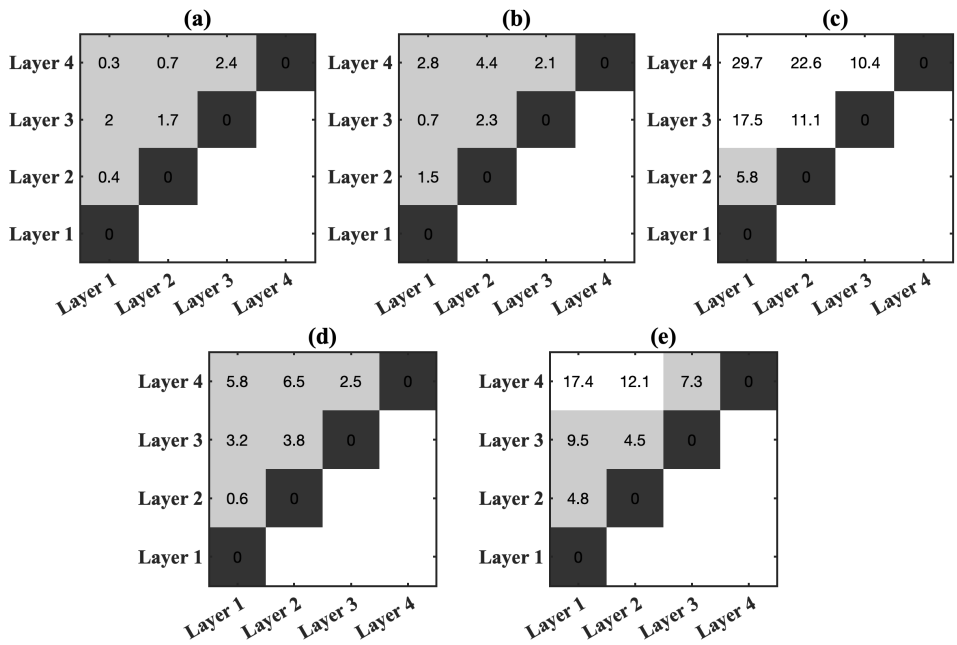

Figure A2. Pairwise SUV_{Mean} Percentage variability matrix for (a) Day 0, (b) Day 1, (c) Day 4, (d) Day 5, (e) Day 6 – White represents the Paris that fail the 10% threshold

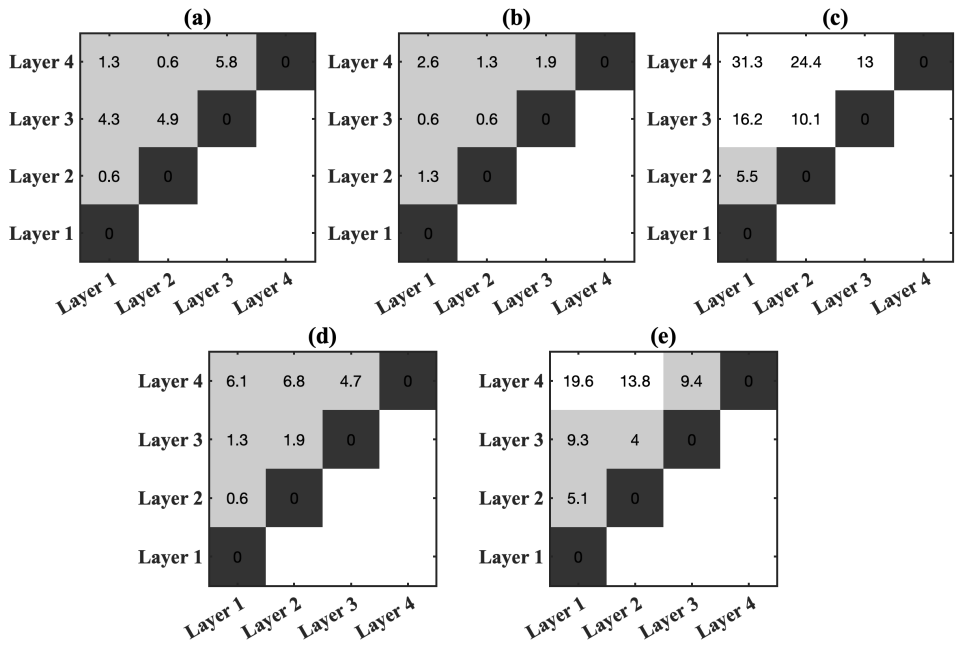

Figure A3. Pairwise SUV_{Max} Percentage variability matrix for (a) Day 0, (b) Day 1, (c) Day 4, (d) Day 5, (e) Day 6 – White represents the Paris that fail the 10% threshold

NOTE: This preprint reports new research that is not certified by peer review and should not be used to guide clinical practice.

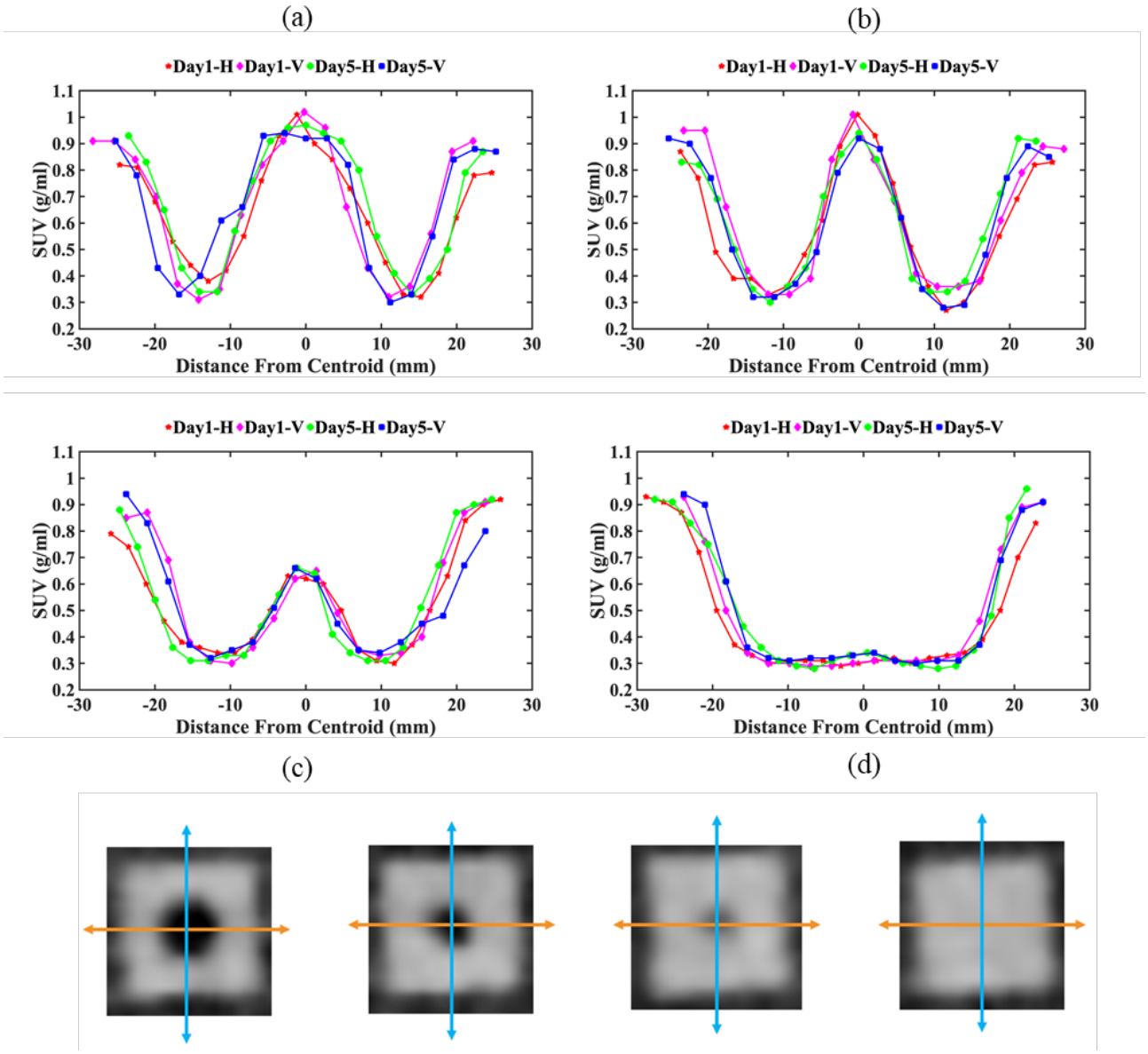

Figure A4. Day 1 vs Day 5 - SUV Profile along Vertical and Horizontal direction vectors from Cube centroid on Axial Plane : (a) 70-5-20, (b) 70-5-15, (c) 70-5-10, (d) 70-5-0; Reference for Profile Extraction on Cropped PET Image (Bottom) – Only Day – 1 and Day – 5 were selected based on highest pairwise Wilcox *p* values , effective activity during first scan and layer variability criteria

NOTE: This preprint reports new research that is not certified by peer review and should not be used to guide clinical practice.

References:

1. Ljungberg M. Instrumentation, Calibration, Quantitative Imaging, and Quality Control. In: Radiotheranostics - A Primer for Medical Physicists I. CRC Press; 2024.

2. McDougald WA, Mannheim JG. Understanding the importance of quality control and quality assurance in preclinical PET/CT imaging. EJNMMI Phys. 2022 Oct 31;9(1):77.

3. Reynés-Llompart G, Zorz A, Boellaard R, Ptáček J, Pike L, Soret M, et al. Quality control in PET/CT and PET/MRI: Results of a survey amongst European countries. Phys Med. 2022 Jul 1;99:16–21.

4. Koole M, Armstrong I, Krizsan AK, Stromvall A, Visvikis D, Sattler B, et al. EANM guidelines for PET-CT and PET-MR routine quality control. Z Für Med Phys. 2023 Feb 1;33(1):103–13.

5. D'Arienzo M, Pimpinella M, Capogni M, De Coste V, Filippi L, Spezi E, et al. Phantom validation of quantitative Y-90 PET/CT-based dosimetry in liver radioembolization. EJNMMI Res. 2017 Dec;7(1):94.

6. Lu S, Zhang P, Li C, Sun J, Liu W, Zhang P. A NIM PET/CT phantom for evaluating the PET image quality of micro-lesions and the performance parameters of CT. BMC Med Imaging. 2021 Dec;21(1):165.

7. Kidera D, Kihara K, Akamatsu G, Mikasa S, Taniguchi T, Tsutsui Y, et al. The edge artifact in the point-spread function-based PET reconstruction at different sphere-to-background ratios of radioactivity. Ann Nucl Med. 2016 Feb 1;30(2):97–103.

8. Munk OL, Tolbod LP, Hansen SB, Bogsrud TV. Point-spread function reconstructed PET images of sub-centimeter lesions are not quantitative. EJNMMI Phys. 2017 Jan 13;4(1):5.

9. Berthon B, Marshall C, Edwards A, Evans M, Spezi E. Influence of cold walls on PET image quantification and volume segmentation: A phantom study. Med Phys. 2013;40(8):082505.

10. Tong S, Alessio A, Thielemans K, Stearns C, Ross S, Kinahan P. Edge artifacts in PSF-based PET image reconstruction: Characterization and mitigation. J Nucl Med. 2011 May 1;52(supplement 1):106–106.

NOTE: This preprint reports new research that is not certified by peer review and should not be used to guide clinical practice.

11. Matheoud R, Boellaard R, Pike L, Ptacek J, Reynés-Llompart G, Soret M, et al. EFOMP's protocol quality controls in PET/CT and PET/MR. Phys Med. 2023 Jan;105:102506.

12. Maronnier Q, Courbon F, Caselles O. Evaluation of a method based on synthetic data inserted into raw data prior to reconstruction for the assessment of PET scanners. EJNMMI Phys. 2022 Oct 1;9(1):68.

13. Tandon P, Prakash D, Kheruka SC, Bhat NN. Quality Assurance in Positron Emission Tomography-Computed Tomography (PET-CT). In: Tandon P, Prakash D, Kheruka SC, Bhat NN, editors. Radiation Safety Guide for Nuclear Medicine Professionals [Internet]. Singapore: Springer Nature; 2022 [cited 2024 Nov 7]. p. 233–65. Available from: https://doi.org/10.1007/978-981-19-4518-2_17

14. Okamoto M, Takahashi K, Oda K, Satoh Y, Inaoka Y, Miyatake H, et al. Dedicated QC/QA phantom tools using traceable Ge-68/Ga-68 point-like sources for dbPET and PEM. J Nucl Med. 2019 May 1;60(supplement 1):2026–2026.

15. Chen MK, Menard DH, Cheng DW. Determining the Minimal Required Radioactivity of 18F-FDG for Reliable Semiquantification in PET/CT Imaging: A Phantom Study. J Nucl Med Technol. 2016 Mar;44(1):26–30.

16. Fahey F, Christian P, Zukotynski K, Sexton-Stallone B, Kiss C, Clarke B, et al. Use of a Qualification Phantom for PET Brain Imaging in a Multicenter Consortium: A Collaboration Between the Pediatric Brain Tumor Consortium and the SNMMI Clinical Trials Network. J Nucl Med. 2019 May;60(5):677–82.

17. Sipilä O, Liukkonen J, Halme HL, Tolvanen T, Sohlberg A, Hakulinen M, et al. Variability in PET image quality and quantification measured with a permanently filled 68Ge-phantom: a multi-center study. EJNMMI Phys. 2023 Jun 16;10(1):38.

18. Gillett D, Marsden D, Ballout S, Attili B, Bird N, Heard S, et al. 3D printing 18F radioactive phantoms for PET imaging. EJNMMI Phys. 2021 Apr 28;8(1):38.

NOTE: This preprint reports new research that is not certified by peer review and should not be used to guide clinical practice.

19. Mínguez Gabiña P, Monserrat Fuertes T, Jauregui I, del Amo C, Rodeño Ortiz de Zarate E, Gustafsson J. Activity recovery for differently shaped objects in quantitative SPECT. Phys Med Biol. 2023 Jun;68(12):125012.

20. Badea RA, Voicu AM, Orian A, Paraschiv B, Vasiliu A, David EC, et al. 3D PRINTED ANTHROPOMORPHIC DOSIMETRIC PHANTOMS RECONSTRUCTED FROM DICOM IMAGES. 2024.

21. Cavaliere C, Baldi D, Brancato V, Aiello M, Salvatore M. A customized anthropomorphic 3D-printed phantom to reproducibility assessment in computed tomography: an oncological case study. Front Oncol. 2023 Aug 28;13:1123796.

22. Cerviño L, Soultan D, Cornell M, Yock A, Pettersson N, Song WY, et al. A novel 3D-printed phantom insert for 4D PET/CT imaging and simultaneous integrated boost radiotherapy. Med Phys. 2017 Oct;44(10):5467–74.

23. Okkalidis N. 3D printing methods for radiological anthropomorphic phantoms. Phys Med Biol. 2022 Jul;67(15):15TR04.

24. Gear JI, Cummings C, Craig AJ, Divoli A, Long CDC, Tapner M, et al. Abdo-Man: a 3D-printed anthropomorphic phantom for validating quantitative SIRT. EJNMMI Phys. 2016 Dec;3(1):17.

25. Gear JI, Long C, Rushforth D, Chittenden SJ, Cummings C, Flux GD. Development of patient-specific molecular imaging phantoms using a 3D printer. Med Phys. 2014 Aug;41(8Part1):082502.

26. Gear JI, Cummings C, Sullivan J, Cooper-Rayner N, Downs P, Murray I, et al. Radioactive 3D printing for the production of molecular imaging phantoms. Phys Med Biol. 2020 Sep 7;65(17):175019.

27. Wollenweber SD, Alessio AM, Kinahan PE. A phantom design for assessment of detectability in PET imaging. Med Phys. 2016;43(9):5051–62.

NOTE: This preprint reports new research that is not certified by peer review and should not be used to guide clinical practice.

28. Lam TO, Young A. Fabrication of 3D Printed Hollow Spheres for QC and Feasibility for Use With xSPECT Bone [Internet]. In Review; 2023 Jul [cited 2024 Jan 25]. Available from: https://www.researchsquare.com/article/rs-3126362/v1

29. Jessen L, Gustafsson J, Ljungberg M, Curkic-Kapidzic S, Imsirovic M, Sjögreen-Gleisner K. 3D printed non-uniform anthropomorphic phantoms for quantitative SPECT. EJNMMI Phys. 2024 Jan 22;11(1):8.

30. Hafiz HM, Noramaliza MN, Hasley RS, Fikri ASF. DEVELOPMENT AND DESIGN OF A 3D-PRINTED PHANTOM FOR PET-CT NUCLEAR IMAGING QUALITY CONTROL: THE FIRST PHASE OF THE STUDY. J Med Imaging Radiat Sci. 2023 Sep 1;54(3, Supplement):S18.

31. Wegner M, Krause D. 3D printed phantoms for medical imaging: recent developments and challenges. J Mech Sci Technol. 2024 Sep 1;38(9):4537–43.

32. Läppchen T, Meier LP, Fürstner M, Prenosil GA, Krause T, Rominger A, et al. 3D printing of radioactive phantoms for nuclear medicine imaging. EJNMMI Phys. 2020 Apr 22;7(1):22.

33. Tang MZ, Choo HL, Yeong CH, Wong YH. Development of 3D-Printed Heterogeneous Tumour Phantom for Quantitative Analysis in PET/CT Imaging. MATEC Web Conf. 2021;335:03014.

34. Gallivanone F, Interlenghi M, D'Ambrosio D, Trifirò G, Castiglioni I. Parameters Influencing PET Imaging Features: A Phantom Study with Irregular and Heterogeneous Synthetic Lesions. Contrast Media Mol Imaging. 2018;2018(1):5324517.

35. Theisen AL, Lassmann M, Tran-Gia J. Toward a Patient-Specific Traceable Quantification of SPECT/CT-Based Radiopharmaceutical Distributions. J Nucl Med. 2022 Jul;63(7):1108.

36. Qiu J, Hou K, Dyer BA, Chen JC, Shi L, Sun Y, et al. Constructing Customized Multimodal Phantoms Through 3D Printing: A Preliminary Evaluation. Front Phys [Internet]. 2021 Apr 27 [cited 2024 Nov 4];9. Available from: https://www.frontiersin.org/journals/physics/articles/10.3389/fphy.2021.605630/full

NOTE: This preprint reports new research that is not certified by peer review and should not be used to guide clinical practice.

37. Asbai-Ghoudan R, Ruiz de Galarreta S, Rodriguez-Florez N. Analytical model for the prediction of permeability of triply periodic minimal surfaces. J Mech Behav Biomed Mater. 2021 Dec;124:104804.

38. Cholifah U, Nafiunisa A, Aryanti N, Wardhani DH. The influence of cocamide DEA towards the characteristics of transparent soap. IOP Conf Ser Mater Sci Eng. 2021 Feb;1053(1):012016.

39. The new opportunities for high time resolution clinical TOF PET | Clinical and Translational Imaging [Internet]. [cited 2025 Mar 17]. Available from: https://link.springer.com/article/10.1007/s40336-019-00316-5

40. Yildirim N, Simsek M, Aldemir MN, Bilici M, Tekin SB. Relationship between 18-FDG-PET/CT and Clinicopathological Features and Pathological Responses in Patients with Locally Advanced Breast Cancers. Eurasian J Med. 2019 Jun;51(2):154–9.

41. Qi C, Wang S, Yu H, Zhang Y, Hu P, Tan H, et al. An artificial intelligence-driven image quality assessment system for whole-body [18F]FDG PET/CT. Eur J Nucl Med Mol Imaging. 2023 Apr 1;50(5):1318–28.

42. Graef J, Senger C, Wetz C, Baur ADJ, Kluge AK, Lukas M, et al. Shortened Tracer Uptake Time in GA-68-DOTATOC-PET of Meningiomas Does Not Impair Diagnostic Accuracy and PET Volume Definition. Diagnostics. 2020 Dec;10(12):1084.

43. Luna CBB, Filho EA dos S, Siqueira DD, Araújo EM, Nascimento EP do, de Mélo TJA. Influence of Small Amounts of ABS and ABS-MA on PA6 Properties: Evaluation of Torque Rheometry, Mechanical, Thermomechanical, Thermal, Morphological, and Water Absorption Kinetics Characteristics. Materials. 2022 Jan;15(7):2502.

44. Leite M, Varanda A, Ribeiro AR, Silva A, Vaz MF. Mechanical properties and water absorption of surface modified ABS 3D printed by fused deposition modelling. Rapid Prototyp J. 2018 Jan 2;24(1):195–203.

45. Yavuz G, Kovan B, Toklu T, Çermik TF, Öztürk C. Calculation of recovery coefficients for partial volume effect correction in PET/CT imaging using a customized anthropomorphic body phantom. Biomed Eng OnLine. 2025 Feb 15;24(1):20.

NOTE: This preprint reports new research that is not certified by peer review and should not be used to guide clinical practice.

46. Aide N, Lasnon C, Veit-Haibach P, Sera T, Sattler B, Boellaard R. EANM/EARL harmonization strategies in PET quantification: from daily practice to multicentre oncological studies. Eur J Nucl Med Mol Imaging. 2017;44(Suppl 1):17–31.

NOTE: This preprint reports new research that is not certified by peer review and should not be used to guide clinical practice.